Composite Structures 352 (2025) 118674

Contents lists available at ScienceDirect

Composite Structures

journal homepage: www.elsevier.com/locate/compstruct

# Crashworthiness assessment of a composite fuselage stanchion employing a strain rate dependent damage model

Mário Miranda [a,*], Andrea Cini [b], Antonio Raimondo [b], Volnei Tita [c,d]

[a] *Department of Aeronautics, Imperial College London, Exhibition Rd, South Kensington, London SW7 2AZ, UK*
[b] *Department of Aerospace Engineering, Universidad Carlos III de Madrid, Madrid 28911, Spain*
[c] *Department of Aeronautical Engineering, Engineering School of São Carlos, University of São Paulo, São Carlos, SP, Brazil*
[d] *Department of Mechanical Engineering, Faculty of Engineering, University of Porto, Porto, Portugal*

## ARTICLE INFO

*Keywords:*
Crashworthiness
Composites
Fuselage
Damage modelling

## ABSTRACT

Numerical testing is crucial for the design of composite fuselages, which have strict crashworthiness regulations. However, the majority of studies on numerical fuselage impacts do not account for the effects of strain rate in simulations. A damage model considering strain rate dependence has been implemented to accurately predict the impact behaviour of a composite fuselage structure. This model enhances the existing three-dimensional Hashin criterion by incorporating strain rate effects and its implemented numerically using a VUMAT subroutine in ABAQUS/explicit. Validation of the model is done through a low-velocity impact problem, showing a better correlation with experimental data compared to previous numerical analyses available in the literature. The study focuses on high-energy impact on a composite stanchion in the lower lobe of an aircraft fuselage. Results demonstrate that the newly proposed model effectively predicts failure zones and modes, indicating its potential in addressing dynamic composite problems typical of impact scenarios.

## 1. Introduction

As the aeronautical industry seeks to increase performance and optimise maintenance costs, Carbon Fibre Reinforced Plastic (CFRP) materials have been incorporated into civil aircraft such as the A350 due to their superior properties, including high specific strength, excellent resistance to corrosion, and extended fatigue life [1–3]. Airworthiness regulations require that no change in occupant safety should occur whether composite or metal structures are employed [4]. As a proof of compliance, manufacturers are required to show either by direct tests or test supported analysis (building block-approach [4,5]) that the aircraft satisfies different criteria, such as retention of items of mass (e.g. overhead bins) or maintenance of a survivable volume [4,6]. Given that experimental tests are costly, manufacturers rely on computational tools such as finite element analysis to evaluate different geometries or design variables such as different number of plies, stacking sequence or even impact orientation and therefore, it is of great interest to employ accurate models to aid the design process [4].

There are many different works on the behaviour of composite structures under impact [7–11], where it is observed that contrarily to metals where energy is absorbed by plastic deformation, the main energy composite absorption mechanisms come for intra (inside the ply) and inter-laminar (delamination) damage [12,13]. To numerically predict these failure modes, researchers have proposed various models [14–17], having some (mostly Hashin [18] and Chang–Chang [19]) been employed in simulating both thin-walled composite columns [20–22] and composite fuselage components under compression and impact scenarios [23–29]. However, for fuselage components, sometimes a noticeable difference is observed between numerical and experimental results. One factor that is rarely present in past studies, and practically not addressed in composite fuselage related problems, is the strain rate effect. Carbon fibres are considered to be practically strain insensitive [30], however, the polymeric material is not, and can influence the behaviour of the laminate, specially under compression [31]. There have been some models proposed to account for the strain rate effect in CFRP [31–33] such as the one proposed by Millen et al. [34]. Although there are some examples in literature of works which incorporate strain rate effects in impact simulations, adjusting the material properties *a priori* [35] or by direct calculation during the analysis [36], their generalised employment in numerical simulations of impact problems is still limited, specially for fuselage components, as pointed out by Liu et al. [37] in their extensive review.

Building on this groundwork, the present study investigates the potential benefits of incorporating strain rate effects into the numerical impact analysis of composite parts and fuselage structures. A 3D Hashin

---

* Corresponding author.
*E-mail address:* m.miranda23@imperial.ac.uk (M. Miranda).

https://doi.org/10.1016/j.compstruct.2024.118674
Received 22 May 2024; Received in revised form 14 October 2024; Accepted 23 October 2024

strain rate dependent failure model based on the strategy employed by Millen et al. [34] is used in the impact simulation of composite parts. The material damage model is introduced as well as the strategy followed to include the strain rate effect. The developed model is verified using a simple one element displacement controlled test. The material model is then validated with a Low Velocity Impact (LVI) problem and bench-marked against experimental and numerical results from the literature. After validating the model, an impact of a composite stanchion is simulated, where the failure mode is studied and the results are compared to documented experimental observations.

The key novelty of this study is the incorporation of strain rate sensitivity in impact simulations of composite structures, which has been largely overlooked in previous works, specially regarding fuselage components (e.g., [23,25,27]). By introducing this feature, this work offers a more accurate and comprehensive framework for predicting material failure under dynamic conditions, which can be applied not only for aeronautical structures, but also for all problems related to crashworthiness analysis.

## 2. Material model

In this section, the material laws employed in this study are presented, beginning with the intra-laminar model and concluding with the inter-laminar damage model. The intra-laminar model is organised in subsections: damage onset (failure criterion), damage evolution, and the effect of strain rate.

### 2.1. Intra-laminar damage

### 2.1.1. Damage onset

To determine the damage onset, a 3D Hashin failure criterion [18] was used, being able to distinguish 4 different failure modes which are defined by the following equations:

- Fibre tensile failure ($\sigma_{11} \geq 0$)

$$F_{ft} = \left(\frac{\sigma_{11}}{X_T}\right)^2 + \alpha\left(\frac{\sigma_{12}}{S_{12}}\right)^2 + \alpha\left(\frac{\sigma_{13}}{S_{13}}\right)^2 \geq 1 \tag{1}$$

- Fibre compressive failure ($\sigma_{11} < 0$)

$$F_{fc} = \left(\frac{\sigma_{11}}{X_C}\right)^2 \geq 1 \tag{2}$$

- Matrix tensile failure ($\sigma_{22} + \sigma_{33} \geq 0$)

$$F_{mt} = \left(\frac{\sigma_{22}+\sigma_{33}}{Y_T}\right)^2 + \frac{1}{S_{23}^2}(\sigma_{23}^2 - \sigma_{22}\sigma_{33}) + \left(\frac{\sigma_{12}}{S_{12}}\right)^2 + \left(\frac{\sigma_{13}}{S_{13}}\right)^2 \geq 1 \tag{3}$$

- Matrix compressive failure ($\sigma_{22} + \sigma_{33} < 0$)

$$F_{mc} = \left(\frac{\sigma_{22}+\sigma_{33}}{2S_{23}}\right)^2 + \frac{\sigma_{22}+\sigma_{33}}{Y_C}\left[\left(\frac{Y_C}{2S_{23}}\right)^2 - 1\right] + \frac{1}{S_{23}^2}(\sigma_{23}^2 - \sigma_{22}\sigma_{33}) + \left(\frac{\sigma_{12}}{S_{12}}\right)^2 + \left(\frac{\sigma_{13}}{S_{13}}\right)^2 \geq 1 \tag{4}$$

where $\sigma_{ij}(i,j = 1,2,3)$ are the stress tensor values, $X_T$, $X_C$, $Y_T$ and $Y_C$ are the tensile and compressive strengths in the fibre and matrix directions respectively. The values $S_{12}$, $S_{13}$ and $S_{23}$ represent the shear strengths in different directions and $\alpha$, is a parameter which controls the influence of the shear stress in tensile failure, which, in this work is set to 1 [38].

### 2.1.2. Degradation model

An energy based linear degradation model was employed, i.e. after damage onset, as seen in Fig. 1 the stiffness decreases linearly so that the total energy equals the fracture energy of the material for that specific failure mode.

In Fig. 1, $\delta^f_{I,eq}$, $\delta^0_{I,eq}$ and $\delta_{I,eq}$ are the equivalent displacements at total failure, damage onset and at the respective time increment, respectively. The values of equivalent displacement and stress are dependent on the failure mode and are defined as follows [39]:

- Fibre tensile failure ($\sigma_{11} \geq 0$)

$$\delta^{ft}_{eq} = l_c\sqrt{\langle\varepsilon_{11}\rangle^2 + \varepsilon_{12}^2 + \varepsilon_{13}^2} \tag{5}$$
$$\sigma^{ft}_{eq} = \frac{l_c(\langle\sigma_{11}\rangle\langle\varepsilon_{11}\rangle + \sigma_{12}\varepsilon_{12} + \sigma_{13}\varepsilon_{13})}{\delta^{ft}_{eq}}$$

- Fibre compressive failure ($\sigma_{11} < 0$)

$$\delta^{fc}_{eq} = l_c\langle-\varepsilon_{11}\rangle \tag{6}$$
$$\sigma^{fc}_{eq} = \frac{l_c\langle-\sigma_{11}\rangle\langle-\varepsilon_{11}\rangle}{\delta^{fc}_{eq}}$$

- Matrix tensile failure ($\sigma_{22} + \sigma_{33} \geq 0$)

$$\delta^{mt}_{eq} = l_c\sqrt{\langle\varepsilon_{22}\rangle^2 + \langle\varepsilon_{33}\rangle^2 + \varepsilon_{12}^2 + \varepsilon_{23}^2 + \varepsilon_{13}^2} \tag{7}$$
$$\sigma^{mt}_{eq} = \frac{l_c(\langle\sigma_{22}\rangle\langle\varepsilon_{22}\rangle + \langle\sigma_{33}\rangle\langle\varepsilon_{33}\rangle + \sigma_{12}\varepsilon_{12} + \sigma_{23}\varepsilon_{23} + \sigma_{13}\varepsilon_{13})}{\delta^{mt}_{eq}}$$

- Matrix compressive failure ($\sigma_{22} + \sigma_{33} < 0$)

$$\delta^{mc}_{eq} = l_c\sqrt{\langle-\varepsilon_{22}\rangle^2 + \langle-\varepsilon_{33}\rangle^2 + \varepsilon_{12}^2 + \varepsilon_{23}^2 + \varepsilon_{13}^2} \tag{8}$$
$$\sigma^{mc}_{eq} = \frac{l_c(\langle-\sigma_{22}\rangle\langle-\varepsilon_{22}\rangle + \langle-\sigma_{33}\rangle\langle-\varepsilon_{33}\rangle + \sigma_{12}\varepsilon_{12} + \sigma_{23}\varepsilon_{23} + \sigma_{13}\varepsilon_{13})}{\delta^{mc}_{eq}}$$

where $l_c$ is the characteristic length, defined by the cubic root of the element volume and $\langle\bullet\rangle$, the Macaulay operator, defined as:

$$\langle a\rangle = \frac{a+|a|}{2}, \forall a \in \mathbb{R} \tag{9}$$

To follow the bi-linear behaviour, each element stiffness matrix needs to be changed once damage is initiated and is represented by the following expression:

$$[C_d] = \frac{1}{\Lambda}\begin{bmatrix} C_{11} & C_{12} & C_{13} & 0 & 0 & 0 \\ C_{21} & C_{22} & C_{23} & 0 & 0 & 0 \\ C_{31} & C_{32} & C_{33} & 0 & 0 & 0 \\ 0 & 0 & 0 & C_{44} & 0 & 0 \\ 0 & 0 & 0 & 0 & C_{55} & 0 \\ 0 & 0 & 0 & 0 & 0 & C_{66} \end{bmatrix} \tag{10}$$

where the subscript $d$ indicates that it is a damaged stiffness matrix, which following the approach used by Zhou et al. [39] (based on Matzenmiller et al. [40]) is defined as follows:

$$C_{11} = d_f E_{11}(1 - d_m\nu_{23}\nu_{32}) \tag{11}$$

$$C_{22} = d_m E_{22}(1 - d_f\nu_{13}\nu_{31})$$

$$C_{33} = E_{33}(1 - d_f d_m\nu_{12}\nu_{21})$$

$$C_{12} = d_f d_m E_{11}(\nu_{21} + \nu_{23}\nu_{31})$$

$$C_{13} = d_f E_{11}(\nu_{31} + d_m\nu_{21}\nu_{32})$$

$$C_{23} = d_m E_{22}(\nu_{32} + d_f\nu_{12}\nu_{31})$$

$$C_{44} = \Lambda d_f d_m G_{12}$$

$$C_{55} = \Lambda d_f d_m G_{23}$$

$$C_{66} = \Lambda d_f d_m G_{13}$$

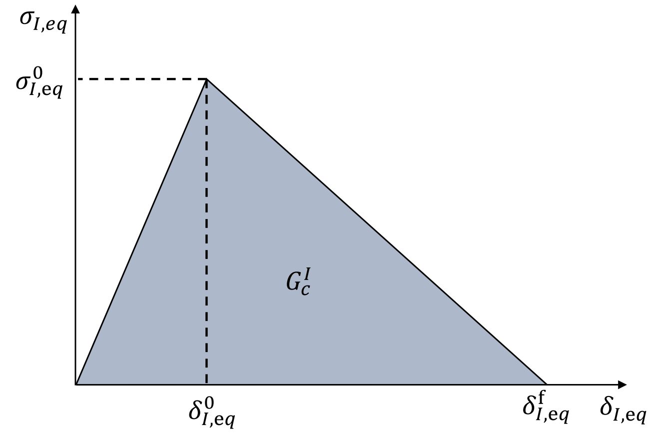

**Fig. 1.** Linear degradation model.

being the damage variables defined as

$$\begin{cases} d_f = (1-d_{ft})(1-d_{fc}) \\ d_m = (1-S_{mt}d_{mt})(1-S_{mc}d_{mc}) \\ \Lambda = 1 - d_f d_m \nu_{12}\nu_{21} - d_m\nu_{23}\nu_{32} - d_f\nu_{13}\nu_{31} - 2d_f d_m \nu_{21}\nu_{32}\nu_{13} \end{cases} \tag{12}$$

where $d_{ft}, d_{fc}, d_{mt}, d_{mc}$ represent different damage variable associated with different failure modes i.e. fibre (aligned with the fibres) and matrix (normal to the fibres) tensile and compressive failure respectively, which values can range from 0 (undamaged) to 1 (fully damaged) and their evolution is given by the following equation:

$$d_I = \frac{\delta^f_{I,eq}(\delta_{I,eq} - \delta^0_{I,eq})}{\delta_{I,eq}(\delta^f_{I,eq} - \delta^0_{I,eq})} \qquad (d_I \in [0,1], I = ft, fc, mt, mc) \tag{13}$$

The values of $S_{mt}$ and $S_{mc}$ are shear stiffness loss control parameters which where set to 0.9 and 0.5 respectively, based on [38].

Given that total failure occurs whenever the total fracture energy is achieved, the equivalent displacement at total failure is determined by:

$$\delta^f_{I,eq} = \frac{2G^I_c}{\sigma^0_{I,eq}} \qquad (I = \{ft, fc, mt, mc\}) \tag{14}$$

where $G_{I_c}$ is the energy release rate of each failure mode, $I$, and $\sigma^0_{I,eq}$ is the equivalent stress level at damage onset, which, in this work, will be defined by the expressions below [39]:

$$\delta^0_{I,eq} = \frac{\delta_{I,eq}}{\sqrt{F_I}} \tag{15}$$

$$\sigma^0_{I,eq} = \frac{\sigma_{I,eq}}{\sqrt{F_I}} \tag{16}$$

where $F_I$ represents the failure index value of the respective failure mode and thus takes values near unity at damage onset.

### 2.1.3. Strain rate effect

To account for the strain rate effect, the approach used by Millen et al. [34] is considered. It consists on using strain rate dependent scaling factors which act on some mechanical properties. Following Millen et al. [34], three different regimes are considered, quasi-static, 0.1 $s^{-1}$, high strain rate, 100 $s^{-1}$, and the intermediate region. From the experimental data available in the literature, the authors were able to determine some mechanical properties for the lower and upper values of strain rate, linearly interpolating the property in the intermediate region following the expression:

$$\beta = \begin{cases} 1.0 \text{ if } \dot{\varepsilon_2} \le 0.1 \\ \dfrac{(\dot{\varepsilon}_2 - 0.1)(1.29-1)}{100-0.1} + 1 \text{ if } 0.1 < \dot{\varepsilon_2} < 100 \\ 1.29 \text{ if } \dot{\varepsilon_2} \ge 100 \end{cases} \tag{17}$$

**Table 1**
Maximum scaling factors ($\dot{\varepsilon_2} \ge 100$) [34].

| | $E_2$ | $G_C^{mc}$ | $G_C^{mt}$ | $X_C$ | $X_T$ | $Y_C$ | $Y_T$ |
|---|---|---|---|---|---|---|---|
| Scaling Factor | 1.29 | 1.63 | 1.23 | 1.39 | 1.38 | 1.37 | 1.38 |

where $\beta$ is the scaling parameter which adjusts the property such as, for instance the transversal stiffness:

$$E_{2f} = \beta E_2 \tag{18}$$

being $E_{2f}$ the effective transversal stiffness. The scaling factors used in this work, based on the work of Millen et al. [34], are shown in Table 1.

For each time step, $t$, the strain rate is calculated by dividing the strain increment by the time increment size, $\Delta t$:

$$\dot{\varepsilon}^t = \frac{\varepsilon^t - \varepsilon^{t-\Delta t}}{\Delta t} \tag{19}$$

after which, the scaling parameter to be applied is calculated using Eq. (17), replacing the already in-place maximum scaling factor (1.29) by the one relative to the property being considered, found in Table 1.

### 2.2. Inter-laminar damage

Inter-laminar damage or delamination is an important failure mode which can significantly degrade the mechanical behaviour of composite parts, mainly when impact is involved [41,42]. In this work, cohesive elements are used to simulate the inter-laminar damage and similarly to the intra-laminar damage behaviour, it also presents an onset and evolution of damage. A quadratic failure based criterion was employed to determine the damage onset:

$$\left\{\frac{\langle t_n\rangle}{t_n^0}\right\}^2 + \left\{\frac{t_s}{t_s^0}\right\}^2 + \left\{\frac{t_t}{t_t^0}\right\}^2 = 1 \tag{20}$$

being $t_i (i = n, s, t)$ the traction forces in the normal and both shear directions to the delamination area respectively while the denominators are each direction corresponding force allowable. Regarding the softening phase i.e. the damage evolution, the damage parameter is determined by the following equation [43]:

$$D = \frac{\delta^f_m(\delta^{max}_m - \delta^0_m)}{\delta^{max}_m(\delta^f_m - \delta^0_m)} \tag{21}$$

where $\delta^0_m$ is the effective displacement at damage initiation, i.e. the value of $\delta^{max}_m$ when Eq. (20) is satisfied, and $\delta^f_m$ is the effective displacement at separation. The maximum equivalent or mixed-mode displacement, $\delta^{max}_m$, is defined as

$$\delta^{max}_m = max\left\{\sqrt{\langle\delta_n\rangle^2 + \delta_s^2 + \delta_t^2}\right\} = max\left\{\sqrt{\langle\delta_n\rangle^2 + \delta^2_{shear}}\right\} \tag{22}$$

and being an energy based degradation failure, the effective displacement at total failure is determined by

$$\delta^f_m = \frac{2G_C}{T^0_m} \tag{23}$$

where $G_C$ is the mixed-mode energy release rate and $T^0_m$ the effective traction, given by:

$$T^0_m = K\delta^0_m \tag{24}$$

being $K$ the penalty stiffness. Fig. 2 shows the different mentioned values.

The mixed mode energy release rate, $G_C$, can be estimated using different strategies. One is the power law criterion [44]:

$$\left\{\frac{G^n}{G^n_C}\right\}^2 + \left\{\frac{G^s}{G^s_C}\right\}^2 + \left\{\frac{G^t}{G^t_C}\right\}^2 = 1 \tag{25}$$

being $G_C = G^n + G^s + G^t$ when the equation is satisfied, or the Benzeggagh and Kenane (B–K) [45] model:

$$G_C = G^n_C + (G^s_C - G^n_C)\left\{\frac{G^S}{G^T}\right\}^\eta \tag{26}$$

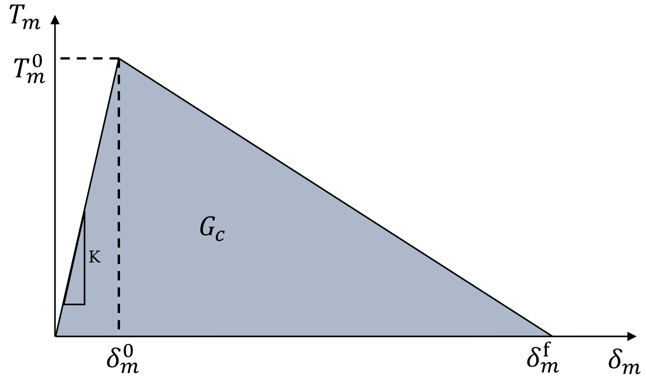

**Fig. 2.** Inter-laminar separation model.

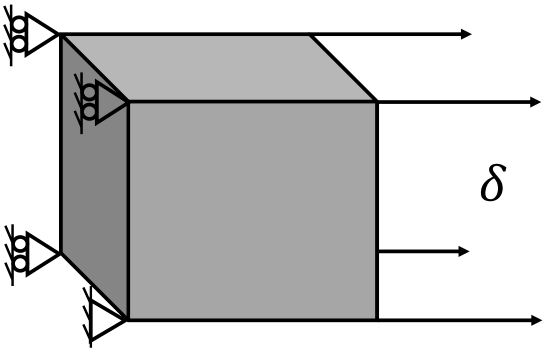

**Fig. 3.** One element test boundary conditions.

where $G^S = G^s + G^t$, $G^T = G^n + G^S$ and $\eta$ is an experimentally obtained parameter which accounts for the mode ratio.

## 3. Numerical implementation and verification

For impact and crash problems, explicit methods are more cost efficient and therefore, explicit FE analyses were developed using Abaqus commercial software. The damage model was implemented using an user-defined material also known as VUMAT subroutine.

Once the code was created, a one element test was preformed for each failure mode individually. The test was carried out for a 1 mm sided cubic C3D8R (three dimensional, 8-noded linear brick element with reduced integration) where for each direction, longitudinal and transverse to the fibres. One of the normal faces is constrained on the load direction and a finite displacement, $\delta$, is imposed at the opposite face, as seen in Fig. 3.

To ensure that failure was achieved for each failure mode, a 10 mm displacement was applied in each direction. Additionally, a node of the constrained face was fixed in order to prevent translational free body movement. Given that the tested failure criterion is strain rate dependent, three different strain rates were applied: quasi-static, intermediate and high strain rate were tested at 0.1 $s^{-1}$, 100 $s^{-1}$ and 10 $s^{-1}$ respectively, being the difference between them the simulation time to achieve the 10 mm displacement. The obtained bi-linear curves are shown in Fig. 4.

As seen from Fig. 4, there is no change in stiffness before damage onset in the longitudinal direction with the change in strain rate whereas the same does not apply to the transverse direction. Furthermore, it is observed that the strain to failure in the longitudinal direction decreases with the increase in strain rate, keeping the area enclosed by the two lines constant for all the different regimes. However, in the transverse directions the energy release rate at fracture changes with the strain rate, and therefore, the failure to strain may increase.

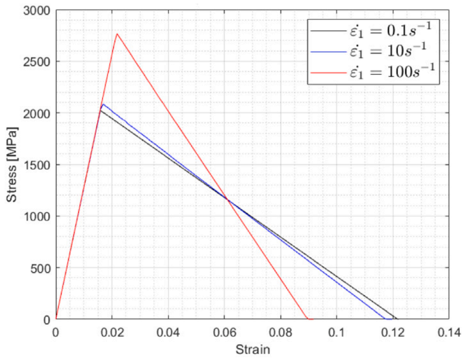

(a) Longitudinal tension

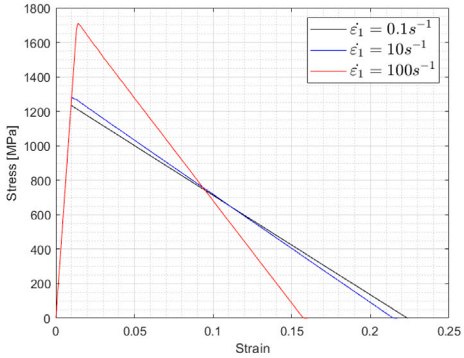

(b) Longitudinal compression

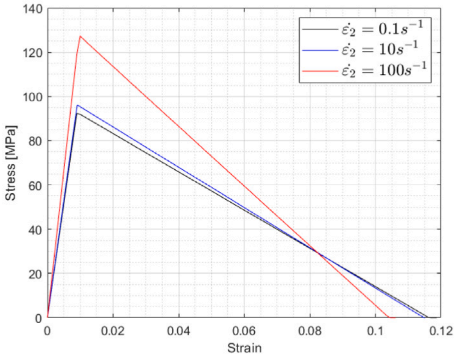

(c) Transverse tension

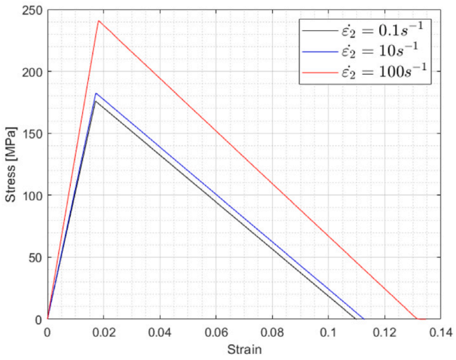

(d) Transverse compression

**Fig. 4.** Bi-linear stress–strain curves at different strain rates.

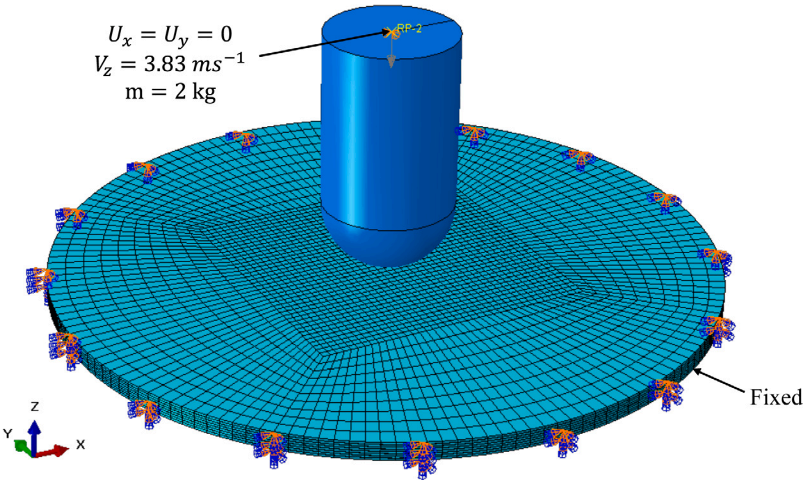

**Fig. 5.** Boundary conditions of the low velocity impact model.

## 4. Material model validation: Low velocity impact

The material model is validated against a well known low velocity impact problem previously studied by different authors [38,39,46].

### 4.1. Low velocity impact model

The model is a cylindrical plate with a diameter of 75 mm and a cross ply $[0/90]_{2S}$ layup, with a layer thickness of 0.25 mm. Additionally, seven cohesive interfaces 0.0075 mm thick were added between each ply. The impactor has a 15 mm diameter hemispherical head and is modelled as an analytical rigid body to reduce simulation costs. The impactor is constrained in all directions but the vertical (Z) to ensure perpendicularity, has a mass of 2 kg and an initial velocity of 3.83 $\mathrm{ms}^{-1}$, for a total impact energy of 14.7 J. The composite plate is clamped at its outer edge as seen in Fig. 5.

The geometry was partitioned to obtain a fully structured mesh with a finer area of 1 × 1 mm brick elements around the impact zone. This mesh size was chosen after a preliminary mesh sensitivity study to obtain a good compromise between mechanical response prediction accuracy and computational time. The mesh size was also aligned with previous studies in the literature [38,46], facilitating a more effective comparison between material models. In total there are 25120 C3D8R elements belonging to the plies and 21980 COH3D8 representing the cohesive interfaces. Table 2 and Table 3 list the material properties of both plies and cohesive elements respectively.

Given that reduced integration elements are being used, a ’RELAX STIFFNESS’ hourglass algorithm [43] with a scaling factor, $s$, set to 1.5 was used, having been selected through an evaluation process considering several metrics ranging from obtained artificial strain energy and computational time. Distortion control and the limitation of the maximum degradation of the cohesive elements to 0.99 were employed to prevent extreme deformation. A general contact algorithm is employed for all parts and plies, including self-contacts, featuring ‘hard’ normal behaviour and penalty-type tangential behaviour. The friction coefficient has been set to 0.5 [38].

### 4.2. Discussion of results

The obtained results (energy–time, force–time, inter and intralaminar damage) are compared to numerical [38,39,46] and experimental [46] data available in the literature in order to evaluate the proposed damage model.

**Table 2**
Material data for numerical impact validation [46].

| Data | Value |
|---|---|
| Density | 1600 kg/m$^3$ |
| $E_1$ (Longitudinal Young’s Modulus) | 153.0 GPa |
| $E_2$=$E_3$ (Transverse Young’s Modulus) | 10.3 GPa |
| $\nu_{12} = \nu_{13}$ (Poisson’s ratio) | 0.3 |
| $\nu_{23}$ (Poisson’s ratio) | 0.4 |
| $G_{12}$=$G_{13}$ (Shear Modulus) | 6.0 GPa |
| $G_{23}$ (Out-of-plane Shear Modulus) | 3.7 GPa |
| $X_T$ (Longitudinal Tensile Strength) | 2537.0 MPa |
| $X_C$ (Longitudinal Compressive Strength) | 1580.0 MPa |
| $Y_T$ (Transverse Tensile Strength) | 82.0 MPa |
| $Y_C$ (Transverse Compressive Strength) | 236.0 MPa |
| $S_{12}$=$S_{13}$ ( Shear Strength) | 90.0 MPa |
| $S_{23}$ (Out-of-plane Shear Strength) | 40.0 MPa |
| $G_C^{ft}$ (Fibre tensile fracture energy) | 91.6 kJ/m$^3$ |
| $G_C^{fc}$ (Fibre compressive fracture energy) | 79.9 kJ/m$^3$ |
| $G_C^{mt}$ (Matrix tensile fracture energy) | 0.22 kJ/m$^3$ |
| $G_C^{ft}$ (Matrix compressive fracture energy) | 1.1 kJ/m$^3$ |

**Table 3**
Material data of the cohesive elements for numerical impact validation [46].

| Data | Value |
|---|---|
| Density | 1600 kg/m$^3$ |
| $E_n$=$E_s$=$E_t$ ( Young’s Modulus) | 5000.0 MPa |
| $T_n = T_s = T_t$ (Normal and shear strengths) | 30.0 MPa |
| $G_C^n$ (Mode I Fracture toughness) | 0.6 N/mm |
| $G_C^s = G_C^t$ (Mode II and III Fracture Toughnesses) | 2.1 N/mm |
| $\eta$ (Mode coupling ratio) | 1.45 |

#### 4.2.1. Energy and force evolution

To obtain the energy absorbed by the plate, the kinetic energy of the impactor is subtracted from the total energy:

$$E_{impactor} = \frac{m}{2} v(t)^2 \tag{27}$$

$$E_{plate} = E_{total} - E_{impactor} \tag{28}$$

where $v(t)$ is the impactor velocity. Fig. 6, shows the comparison between the numerical simulation results and the experimental and numerical analysis performed by Shi et al. [46] and Shao et al. [38] respectively.

As observed in Fig. 6, the proposed model was not only able to replicate the characteristic energy evolution of this impact problem but also to obtain a better prediction relatively to the experimental results. Analysing the initial part of the curve (t≤1 ms), representing the contact of the impactor with the plate, it is possible to observe that the obtained

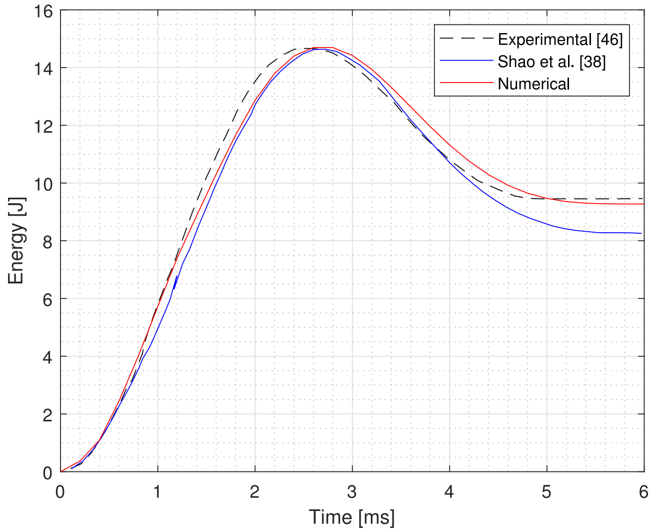

**Fig. 6.** Energy–time curves.

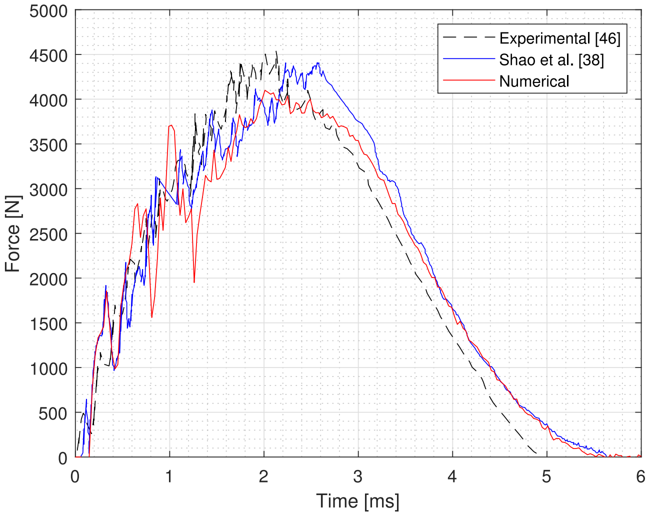

**Fig. 7.** Force–time curves.

**Table 4**
Literature and obtained absorbed energy values.

| Studies | Experimental [J] | Numerical [J] | Error (%) |
|---|---|---|---|
| Shi et al. [46] | 9.52[46] | 9.08 | 4.62 |
| Shao et al. [38] | | 8.25 | 13.34 |
| Zhou et al. [39] | | 8.85 | 7.04 |
| Present study | | 9.27 | 2.63 |

energy is closer to the experimental value, this can be explained by the increased stiffness that the strain rate dependent model brings, leading to an increased value of internal energy compared to other models. After all the kinetic energy is absorbed by the sample (peak), part of the elastic energy absorbed by the plate is returned to the impactor, decreasing the stored energy and reaching a plateau near the 5 ms mark. This value, represents the total impact energy absorbed the composite plate, which the numerical model was able to closely predict. Table 4 lists different absorbed energies obtained by different studies. It can be observed that the present study managed to achieve the better prediction relatively to the experimental value.

One other common metric in this type of problem is the force–time response which is obtained by summing the reaction force in the impact direction (z-axis) of all the fixed nodes of the plate. This curve is characterised by an initial steep increase in reaction force due to the impact which then peaks and goes back to zero, known as the rebound phase of the impactor as shown in Fig. 7.

Although there is an around 9% under-prediction of the maximum force value, it can be observed that there is a good agreement between the obtained numerical and the experimental results, especially on the peak time and rebound phase.

### 4.2.2. Damage area analysis

The damage distribution of different failure modes is presented and compared to previous models and experimental results. Fig. 8 compares the numerically predicted delaminated area to that obtained experimentally by Shi et al. [46] showing a good agreement between the two. The delamination damage, i.e. $D$ of Eq. (21), is presented as the SDEG (Stiffness Degradation) parameter.

The distribution of matrix tensile damage was also compared to previously obtained numerical results to benchmark the proposed damage model (Fig. 9).

The overall shape of the damaged zones aligns with findings from previous studies, yet notably, some layers exhibit slightly smaller damaged areas, which is counterintuitive given the higher energy absorption levels observed in the energy–time evolution. This discrepancy can be attributed to the strain rate effect. At higher strain rates, the matrix stiffness and fracture energy increase, leading to a smaller damaged area for the same level of absorbed energy.

Building on previous studies and literature, these findings validate the effectiveness of the developed damage model in accurately predicting impact-related engineering problems.

## 5. Material model application: Stanchion impact simulation

The principal subject of analysis in this work is a composite stanchion (part of the fuselage floor support), which has previously been studied numerically and experimentally by several researchers [47–49].

### 5.1. Finite element model

The stanchion has a C shaped cross section with geometric details depicted in Fig. 10.

The total thickness is 2.79 mm being the layup [45/-45/90/-45/45/0/0/0/0/0/45/-45/90/-45/45] with 0.005 mm cohesive element interfaces between each ply. In order to have a better direct comparison with previous numerical results, the power law criterion (Eq. (25)) was used, instead of the B–K. The lamina and cohesive element properties are shown in Tables 5 and 6 respectively.

A structured mesh with 4 mm three-dimensional linear brick elements with reduced integration (C3D8R), capable of capturing a three-dimensional stress state, were employed for each composite ply, accompanied by COH3D8 for the cohesive interfaces. Given that the experimental specimen [48] was potted in epoxy resin at its extremities (at a depth of 25.4 mm each), the outer nodes of those zones were enforced a $U_x = U_y = 0$ translational constraint, while the bottom face was fixed (Fig. 11).

The contact algorithm was the same as the one previously employed in the circular plate impact and all the intra-laminar damage variables were limited to 0.95 to prevent numerical issues. A quasi-static compression test was performed to assess if the stiffness was in accordance with experimental results. Table 7 lists the stiffness calculated with the quasi static compression analysis.

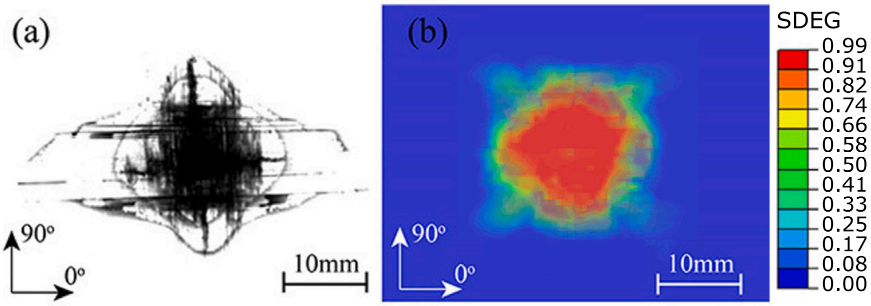

**Fig. 8.** Delamination distribution: (a) X-ray radiograph and (b) numerically predicted (SDEG as delamination damage variable).
*Source:* Adapted from [38].

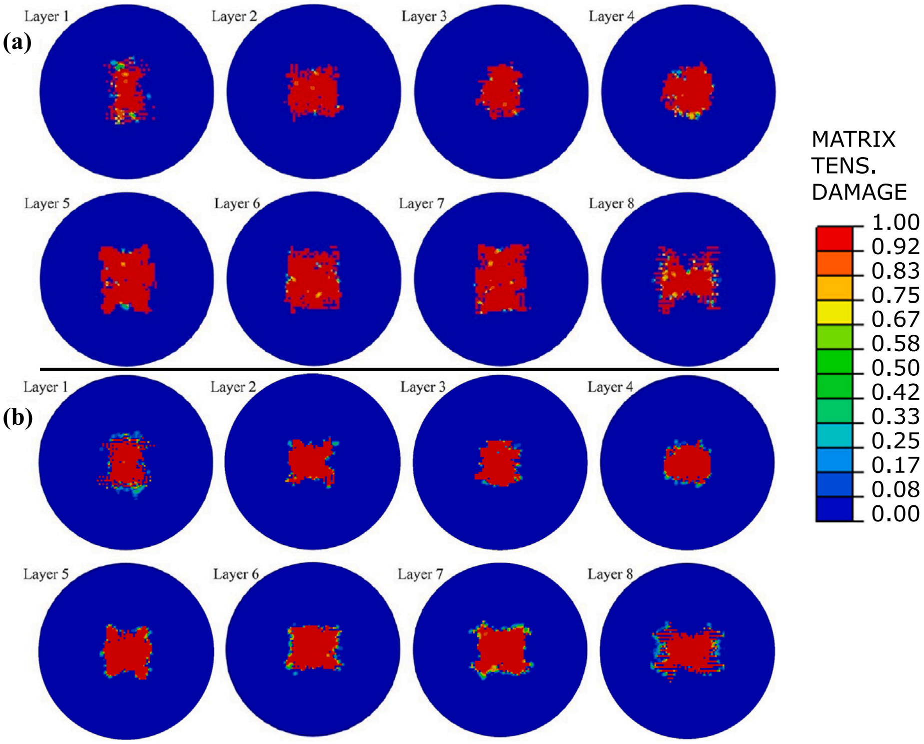

**Fig. 9.** Matrix tensile damage for each composite layer: (a) Shao et al. (b) numerically predicted.
*Source:* Adapted from [38].

### 5.2. Impact test

To simulate a high energy impact, a 15 ms crash event was simulated, where a plate shaped impactor, modelled as an analytical body, was set 0.3 mm away from the top face. The impactor had a mass of 77 kg and an initial vertical velocity of 3.9 ms$^{-1}$ resulting in an impact energy of 585 J (Fig. 12).

Given that manufacturing processes are not perfect and can significantly change the behaviour of shells under compression [50], a linear buckling analysis was run and the first buckling mode multiplied by a factor of 0.05 was introduced as initial perturbation to the structure.

### 5.3. Results and discussion

The deformed shapes of the structure at different times steps are shown in Fig. 13.

From a preliminary observation it can be stated that the failure of the stanchion occurred near the bottom potting region where significant level of delamination occurred. From a more detailed analysis, it was observed that 0.6 ms after impact, the fibres of the 0°central block of the laminate completely failed under compression due to the high crushing loads, as shown in Fig. 14, where the fibre compression damage variable achieves its maximum mainly in the middle of the laminate. Moreover, complete separation took place between the 0°and the 45°plies due to the high shear stresses induced by the significant difference in stiffness.

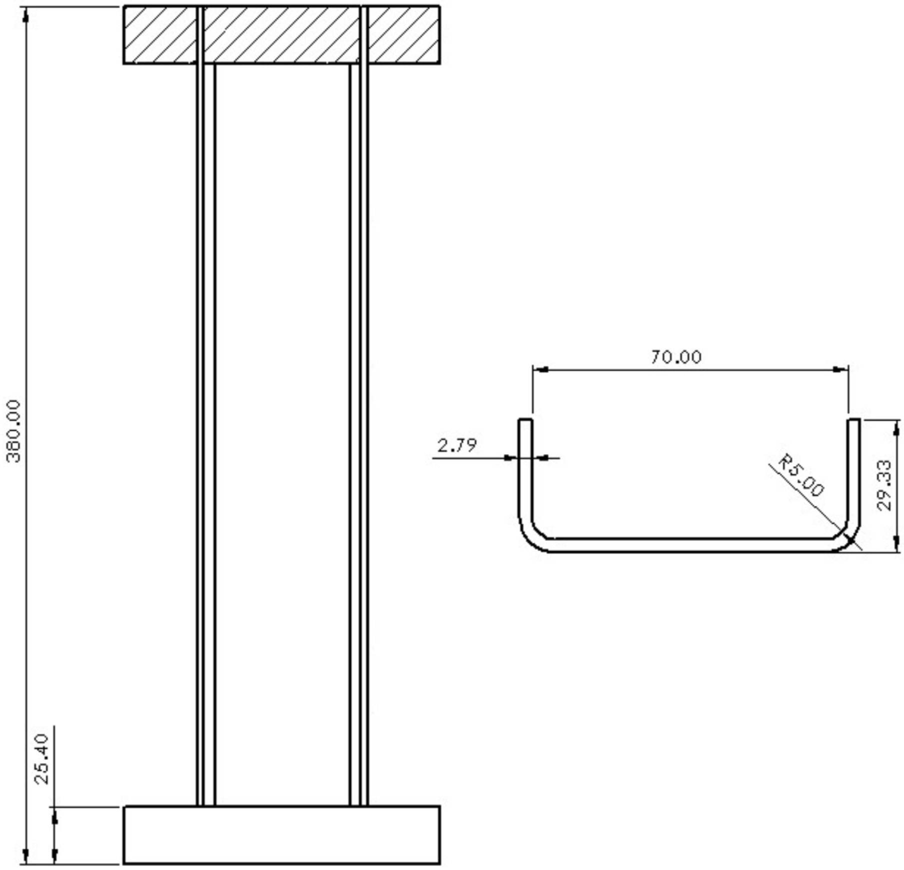

**Fig. 10.** Stanchion geometry (dimmensions in [mm]).

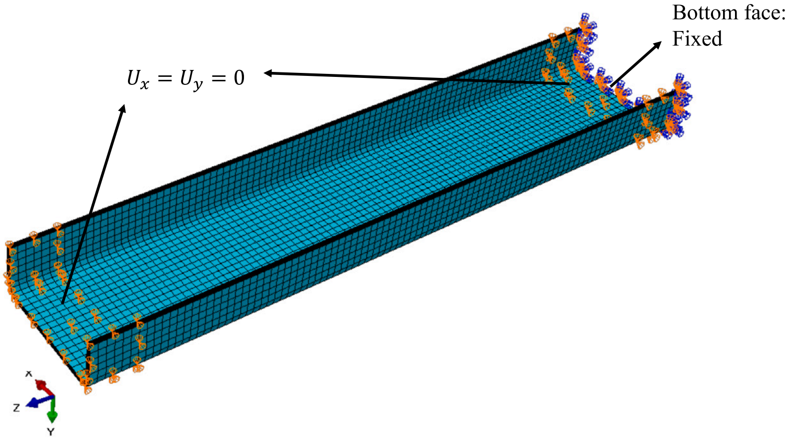

**Fig. 11.** Boundary conditions of the stanchion model.

The continuing crushing force then leads to the matrix compression failure of the outer sets of plies, which are the remaining load carrying plies after the initial failure of the central block. A graph showing the different damage variables through the thickness at t=0.825 ms after impact is shown in Fig. 15. The generalised loss of stiffness promotes a local buckling behaviour (documented failure mode of composite c-stanchions [51]), which is already noticeable to some degree in Fig. 15(a), after which, the shear induced delaminations propagate due to ply buckling and the structure practically entirely loses load carrying capabilities.

### 5.3.1. *Comparison with experimental results*

To evaluate the predictive capabilities of the developed model, a comparison with real test data is performed. The experimental results after impact are shown in Fig. 16(a), where a significant amount of damage can be seen near the potting region. Alternatively, the obtained numerical results are shown in Fig. 16(b), where the elements inside the bottom potting region were hidden for the sake of clarity.

As seen in Fig. 16, there is an excellent agreement in relation to the critical zone, where in the numerical mode is characterised by the aforementioned local buckling onset already evident in Fig. 16(b). Furthermore, recalling the damage distribution in Fig. 15, it is possible

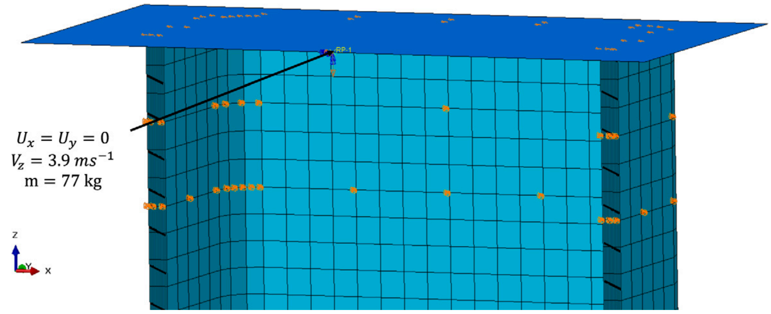

**Fig. 12.** Rigid impactor.

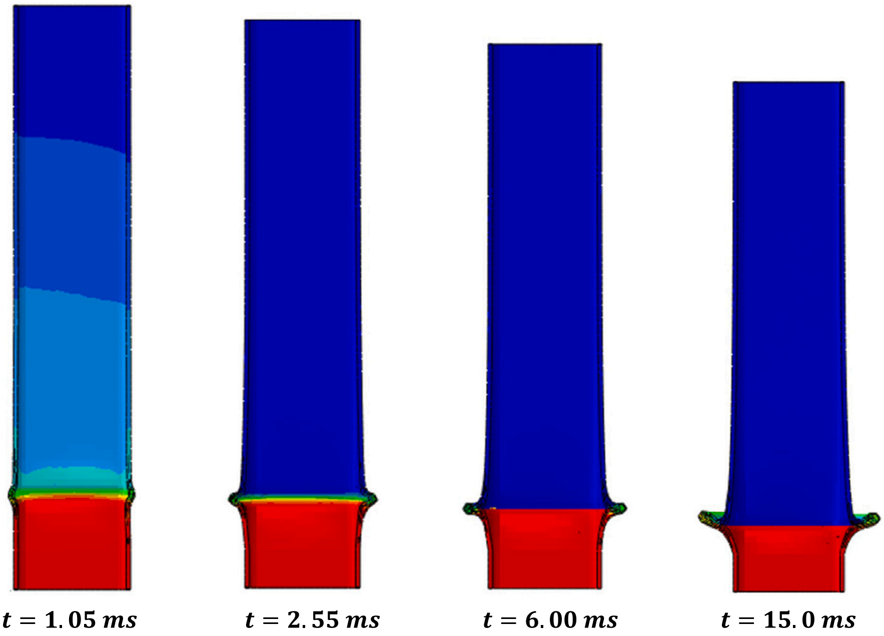

**Fig. 13.** Deformation at different time steps.

**Table 5**
Material data of the stanchion laminae [47].

| Data | Value |
|---|---|
| Density | 1600 kg/m$^3$ |
| E$_1$ (Longitudinal Young's Modulus) | 137.0 GPa |
| E$_2$=E$_3$ (Transverse Young's Modulus) | 8.43 GPa |
| $\nu_{12} = \nu_{13}$ (Poisson's ratio) | 0.26 |
| $\nu_{23}$ (Poisson's ratio) | 0.4 |
| G$_{12}$=G$_{13}$ (Shear Modulus) | 4160.0 MPa |
| G$_{23}$ (Out-of-plane Shear Modulus) | 3328.0 MPa |
| X$_T$ (Longitudinal Tensile Strength) | 2256.0 MPa |
| X$_C$ (Longitudinal Compressive Strength) | 800.0 MPa |
| Y$_T$ (Transverse Tensile Strength) | 100.0 MPa |
| Y$_C$ (Transverse Compressive Strength) | 171.0 MPa |
| S$_{12}$=S$_{13}$ ( Shear Strength) | 85.0 MPa |
| S$_{23}$ (Out-of-plane Shear Strength) | 40.0 MPa |
| $G_C^{ft}$ (Fibre tensile fracture energy) | 47.58 kJ/m$^3$ |
| $G_C^{fc}$ (Fibre compressive fracture energy) | 6.01 kJ/m$^3$ |
| $G_C^{mt}$ (Matrix tensile fracture energy) | 1.53 kJ/m$^3$ |
| $G_C^{ft}$ (Matrix compressive fracture energy) | 4.48 kJ/m$^3$ |

**Table 6**
Material data of the cohesive interfaces of the stanchion [47].

| Property | Value |
|---|---|
| Density | 1600 kg/m$^3$ |
| E$_n$=E$_s$=E$_t$ ( Young's Modulus) | 100000 MPa |
| $T_n$ (Normal Strength) | 27.5 MPa |
| $T_s = T_t$ (Shear Strengths) | 60.0 MPa |
| $G_C^n$ (Mode I Fracture Toughness) | 0.288 N/mm |
| $G_C^s = G_C^t$ (Mode II and III Fracture Toughnesses) | 0.61 N/mm |

**Table 7**
Stanchion stiffness [49].

| Studies | Experimental [kN/mm] | Numerical [kN/mm] | Error (%) |
|---|---|---|---|
| Sellitto et al. [49] | 54.8[49] | 56.3 | 2.6 |
| Present study | | 54.673 | 0.23 |

to observe that some damage modes were accurately predicted, such as delaminations and fibre breakage.

Comparing the obtained numerical results (Fig. 17) with other results from the literature (Fig. 18), it is observed that instead of a diffused damaged area, a highly localised failure zone was predicted, closer resembling experimental results. The different deformed shape is due to the local buckling phenomenon, which was not registered in the previous study.

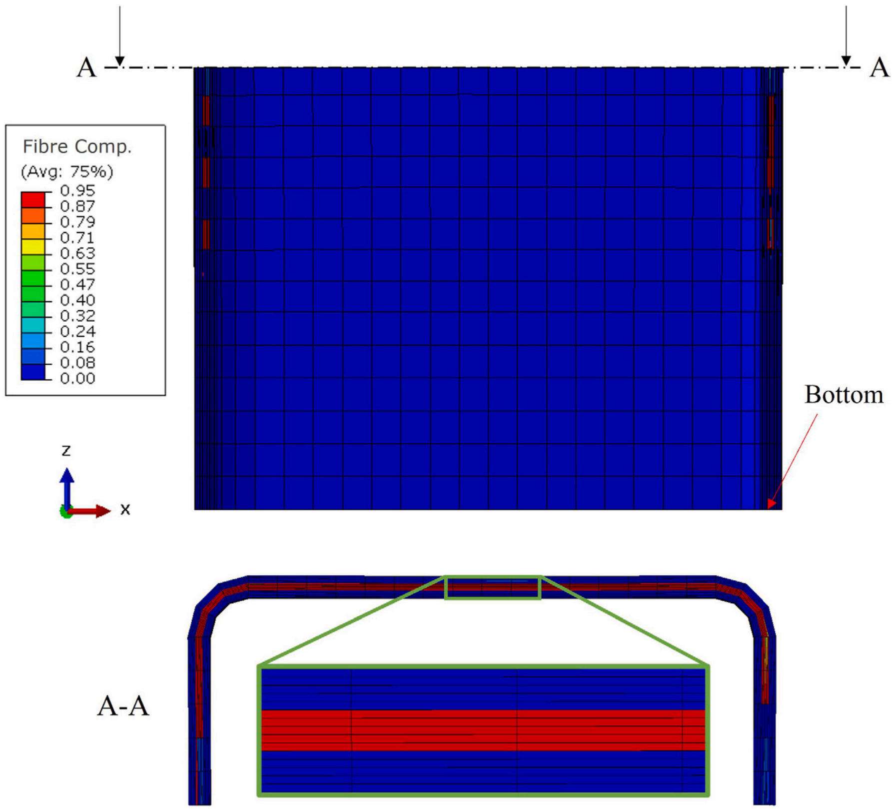

**Fig. 14.** Initial fibre compression failure at the central ply block (t= 0.6 ms after impact).

Although the results obtained differ significantly from those in the literature [47], it is not certain that this discrepancy can be entirely attributed to the inclusion of the strain rate. This uncertainty arises because different elements, such as continuum shell and different number of element through the thickness, were used in the previous analysis. The used material model is also not exactly the same, which can add to those differences.

### 5.3.2. *Strain rate effect*

To evaluate the influence of the strain rate, the same simulation was run neglecting its effect i.e. setting the values of the scaling parameters to 1. Figs. 19 and 20 compare the fibre and matrix damage distribution at the bottom of the stanchion, respectively, at a specific time step, where it is possible to observe that there is a significant damage severity increase, when considering the effect of the strain rate. This change in damage distribution can be explained by a stiffening effect [52] caused by the strain rate inclusion, leading to the embrittlement of the structure [53].

It can also be observed that the local buckling onset zone changes when using a strain insensitive failure model, which is due to the change of the spot with higher generalised loss of stiffness. Therefore, leading to a less accurate prediction relatively to the strain rate dependent model, which presented excellent correlation to the experimental results.

### 5.3.3. *Crashworthiness metrics*

In order to assess the crashworthiness performance of the stanchion and the effect of the strain rate in the simulation, the impactor kinetic energy and acceleration are plotted in Figs. 21(a) and 21(b) respectively, being the latter compared to the experimental results obtained by Riccio et al. [47].

The initial loss of kinetic energy is similar in both models and comes from its conversion into strain and fracture energy of the stanchion. After losing load carrying capabilities (around 1 ms after impact), the kinetic energy loss decreases at a lower rate, due to the buckling of the structure. However, the rate at which the kinetic energy decreases is not the same between models. This difference in due to the different local buckling onset zones and the different deformation behaviour they cause, leading to a more progressive and stable evolution of the non-strain rate dependent model, which is then able to absorb more energy than a structure with unstable failure. The maximum acceleration value was obtained when employing the strain rate dependent model, 148 g, which is approximately 24% less than the experimental predicted value, however, it is closer than the one obtained employing the non-strain rate dependent model, where a value of 141 g was registered. This difference is attributed to the already mentioned stiffening effect. Additionally, it was found that these values were significantly sensible to the number of field output frequency, meaning that numerical time sampling under-prediction might have taken place.

One other common metric in crashworthiness is the force–displacement [51], which is plotted in Fig. 22.

The force–displacement curves reveals a sharp peak followed by a quick decline, ultimately stabilising around 12 kN. Notably, the strain rate dependent model reaches a maximum value of 93.75 kN, which is predictably greater than that of the strain rate insensitive model, 90.39 kN, due to the highest value of maximum acceleration of the former. It can also be observed that the values at the stable crushing zone, where the higher amount of energy is absorbed [54], are generally higher when applying the non-strain rate dependent, which is verified by calculating the mean force, defined as:

$$F_{mean} = \frac{\int F\,dl}{L} \tag{29}$$

where F is the force and L the total crushing distance. Additionally, the Specific Energy Absorption (SEA) [51] can be obtained:

$$SEA = \frac{F_{mean}}{\rho A} \tag{30}$$

where $\rho$ is the density and $A$ the cross sectional area. A summary of the crashworthiness metrics is shown in Table 8.

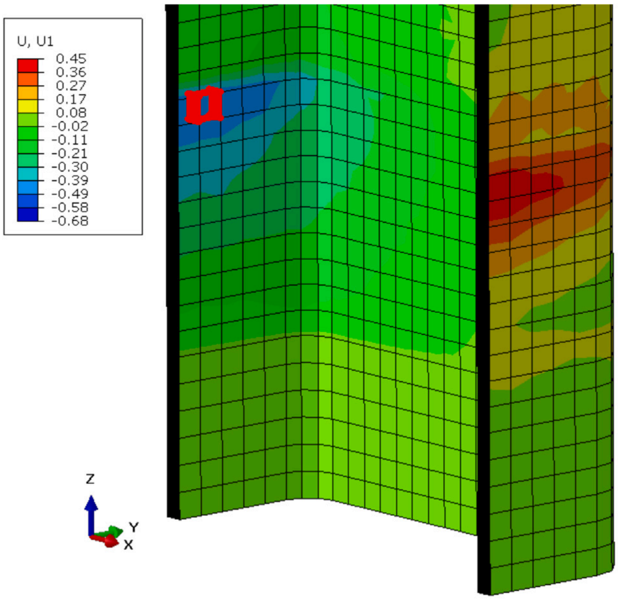

(a)

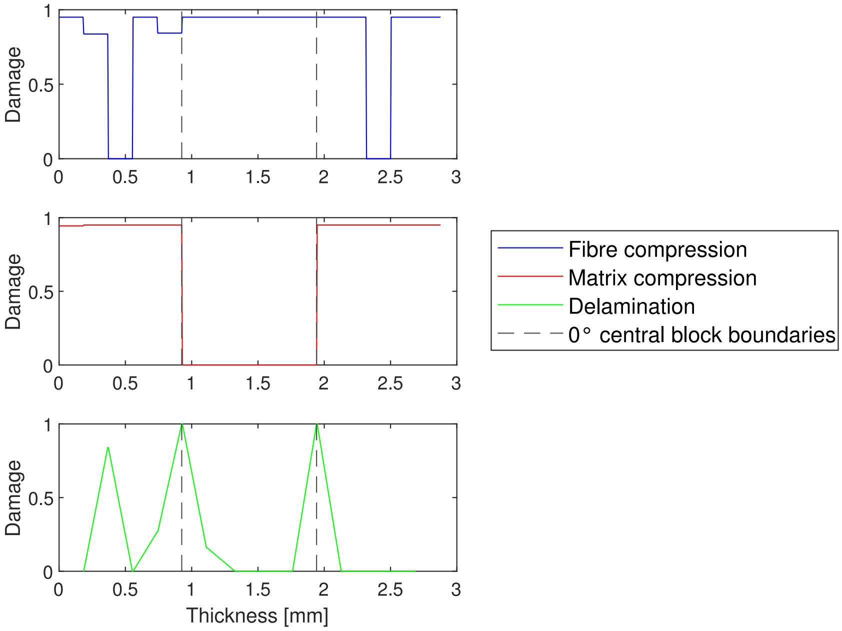

(b)

**Fig. 15.** (a) Element in the local buckling onset zone and (b) respective damage variables through its thickness (t= 0.825 ms after impact).

**Table 8**
Summary of crashworthiness metrics.

| Criterion | $F_{max}$ | $F_{mean}$ | SEA |
|---|---|---|---|
| Non-strain rate | 90.39 kN | 20.56 kN | 37.69 kJ/kg |
| Strain rate | 93.75 kN | 15.70 kN | 28.77 kJ/kg |

As seen in Table 8, the non-strain rate dependent model leads to a higher mean force and consequently, a higher SEA, which was already expected from the kinetic energy evolution (Fig. 21(a)).

## 6. Conclusions

A three-dimensional, strain rate-dependent Hashin composite damage model is introduced and numerically implemented using a VUMAT subroutine to enhance the simulation of impact problems, with particular focus on composite fuselage components. This model is benchmarked against a well-documented low-velocity impact problem and demonstrates improved prediction accuracy compared to experimental results, reducing the absorbed energy value prediction error by at least 43% relatively to previous studies, primarily due to the incorporation

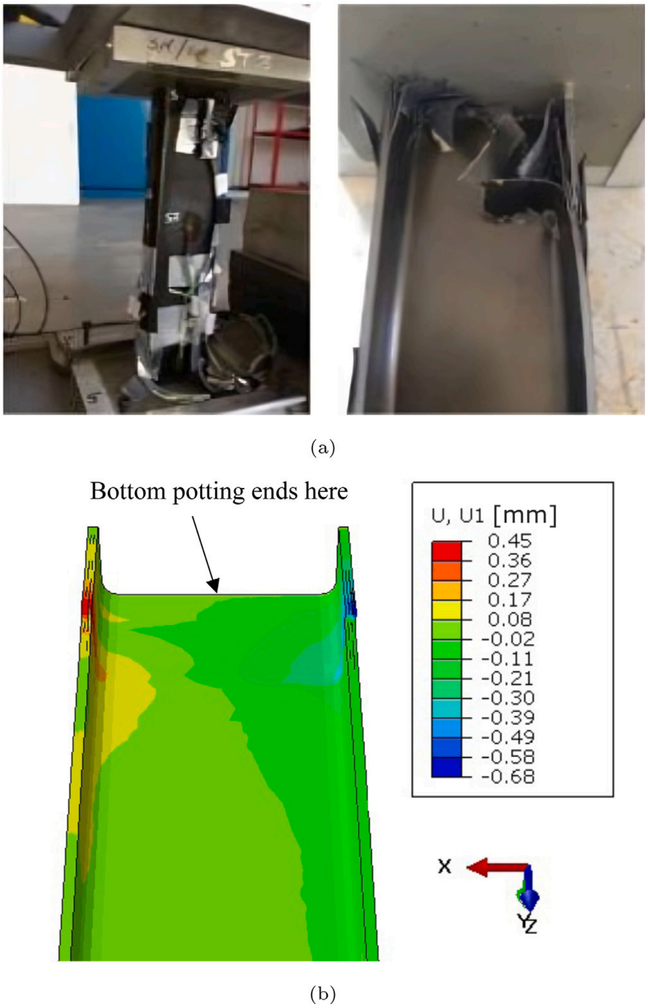

(a)

(b)

**Fig. 16.** (a) Stanchion at the end of experimental test [48] and (b) numerical results (t= 0.825 ms after impact).

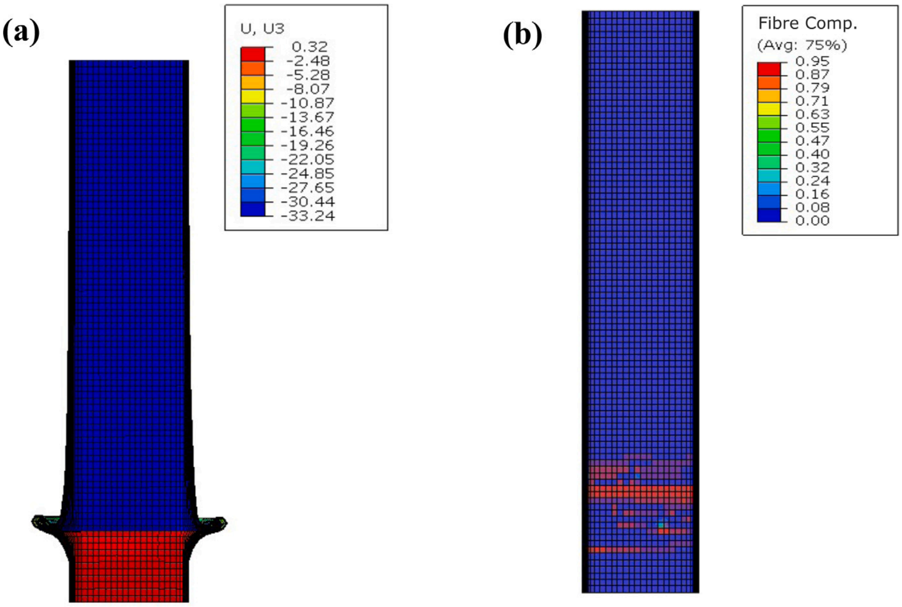

**Fig. 17.** Numerical (a) vertical displacement and (b) undeformed fibre compressive damage distribution with transparency.

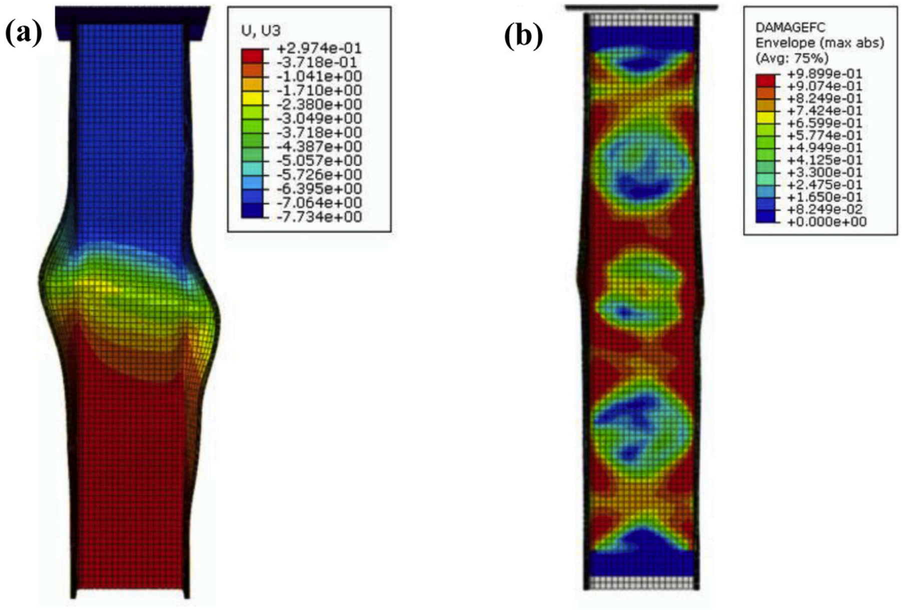

**Fig. 18.** Literature (a) vertical displacement at maximum compression and (b) fibre compressive damage distribution [47].

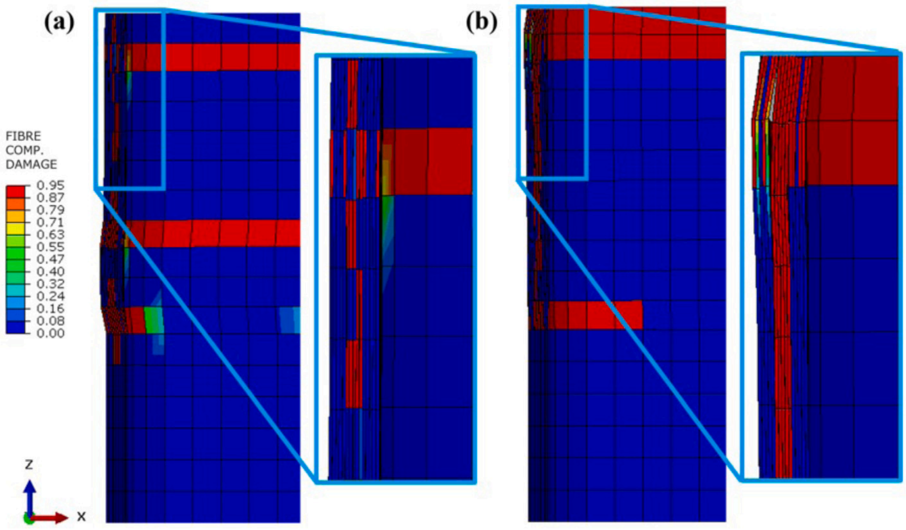

**Fig. 19.** (a) Non-strain rate and (b) strain rate dependent compressive fibre damage (t= 0.825 ms after impact).

of the strain rate effect. The damage model is also applied to simulate a high-energy impact on a composite stanchion of a fuselage structure documented in the literature. The numerical results show excellent agreement with experimentally observed damaged zones and failure modes. It leads to an increase in accuracy compared to previous studies and to the same numerical model employing a strain rate insensitive damage law, increasing the predicted value of peak force by nearly 4%. In conclusion, the introduced three-dimensional strain rate-dependent Hashin failure model proves to be highly effective for accurately predicting composite fuselage impact problems, indicating that incorporating strain rate effects could be beneficial for future simulations.

## CRediT authorship contribution statement

**Mário Miranda:** Writing – review & editing, Writing – original draft, Visualization, Methodology, Investigation, Formal analysis. **Andrea Cini:** Writing – review & editing, Supervision, Resources, Conceptualization. **Antonio Raimondo:** Writing – review & editing, Supervision, Conceptualization. **Volnei Tita:** Writing – review & editing, Supervision, Conceptualization.

## Declaration of competing interest

The authors declare that they have no known competing financial interests or personal relationships that could have appeared to influence the work reported in this paper.

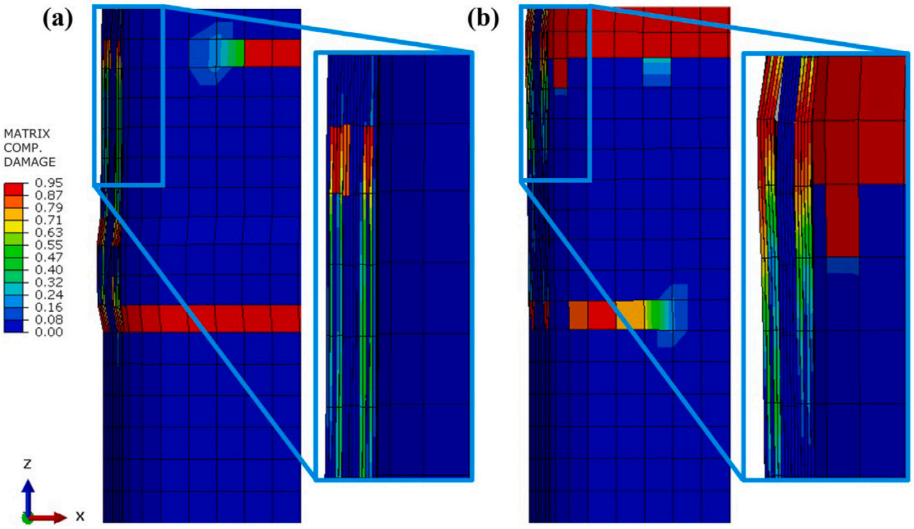

**Fig. 20.** (a) Non-strain rate and (b) strain rate dependent compressive matrix damage (t= 0.825 ms after impact).

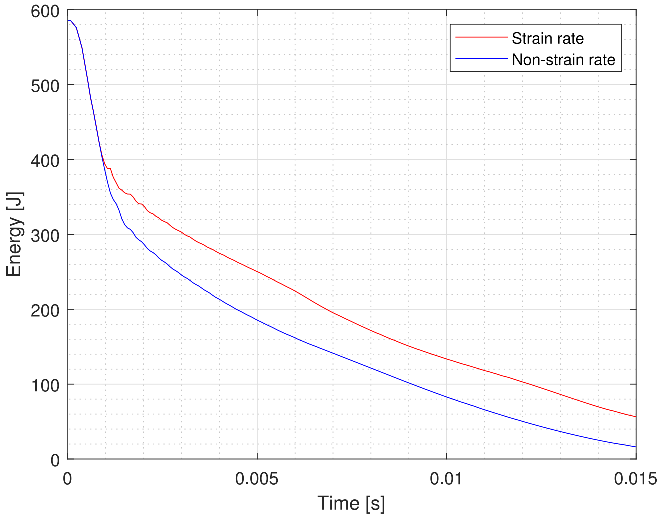

(a) Kinetic energy

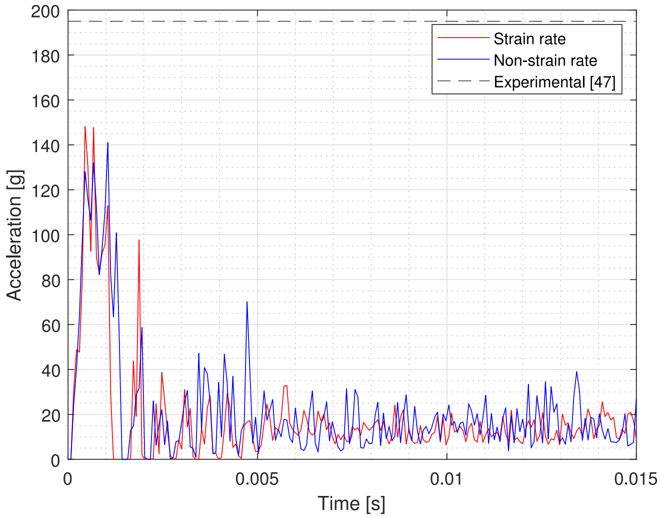

(b) Acceleration

**Fig. 21.** Evolution of impactor (a) kinetic energy and (b) acceleration employing both strain rate and non-strain rate dependent models.

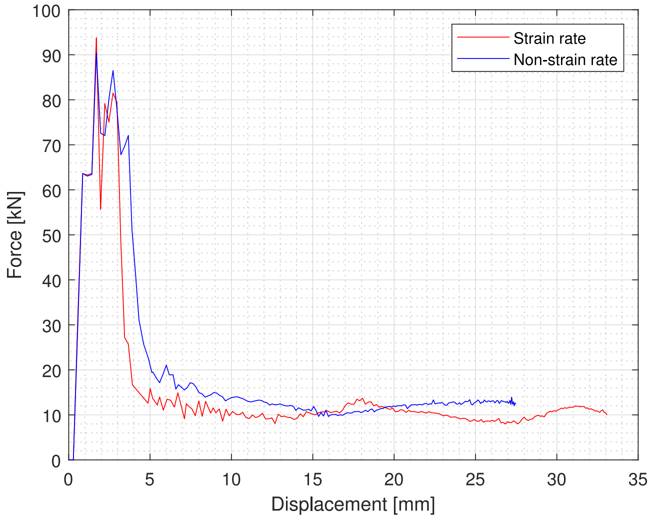

**Fig. 22.** Force–displacement curves employing both strain rate and non-strain rate dependent models.

## Data availability

No data was used for the research described in the article.

## References

[1] Potes F, Silva J, Gamboa P. Development and characterization of a natural lightweight composite solution for aircraft structural applications. Compos Struct 2016;136:430–40. http://dx.doi.org/10.1016/j.compstruct.2015.10.034, URL https://www.sciencedirect.com/science/article/pii/S0263822315009666.

[2] Guo F, Xiao Q, Xiao S, Wang Z. Assembly technology for aeronautical CFRP structures under the collaborative constrains of geometric shape, physical performance and service stability. Compos Struct 2023;318:117071. http://dx.doi.org/10.1016/j.compstruct.2023.117071, URL https://www.sciencedirect.com/science/article/pii/S0263822323004154.

[3] Barreira-Pinto R, Carneiro R, Miranda M, Guedes RM. Polymer-matrix composites: Characterising the impact of environmental factors on their lifetime. Materials 2023;16(11). http://dx.doi.org/10.3390/ma16113913, URL https://www.mdpi.com/1996-1944/16/11/3913.

[4] Federal Aviation Administration. Composite aircraft structure. U.S. Department of Transportation; 2009, Advisory Circular No. 20-107B, URL https://www.faa.gov.

[5] US Department of Defense. Composite materials handbook. Polymer matrix composites materials usage, design, and analysis, vol. 3, 2002.

[6] Federal Aviation Administration. Special conditions No. 25-537-SC. U.S. Department of Transportation; 2014, Special Conditions issued for aircraft certification.

[7] Mamalis AG, Manolakos D, Demosthenous G, Ioannidis M. Crashworthiness of composite thin-walled structures. CRC Press; 2017.

[8] Obradovic J, Boria S, Belingardi G. Lightweight design and crash analysis of composite frontal impact energy absorbing structures. Compos Struct 2012;94(2):423–30. http://dx.doi.org/10.1016/j.compstruct.2011.08.005, URL https://www.sciencedirect.com/science/article/pii/S0263822311002972.

[9] Hull D. A unified approach to progressive crushing of fibre-reinforced composite tubes. Compos Sci Technol 1991;40(4):377–421.

[10] Bisagni C. Experimental investigation of the collapse modes and energy absorption characteristics of composite tubes. Int J Crashworthiness 2009;14(4):365–78. http://dx.doi.org/10.1080/13588260902792954, arXiv:https://doi.org/10.1080/13588260902792954.

[11] Saito H, Chirwa E, Inai R, Hamada H. Energy absorption of braiding pultrusion process composite rods. Compos Struct 2002;55(4):407–17. http://dx.doi.org/10.1016/S0263-8223(01)00160-X, URL https://www.sciencedirect.com/science/article/pii/S026382230100160X.

[12] Aktaş M, Atas C, İçten BM, Karakuzu R. An experimental investigation of the impact response of composite laminates. Compos Struct 2009;87(4):307–13. http://dx.doi.org/10.1016/j.compstruct.2008.02.003, URL https://www.sciencedirect.com/science/article/pii/S0263822308000354.

[13] Liu P, Liao B, Jia L, Peng X. Finite element analysis of dynamic progressive failure of carbon fiber composite laminates under low velocity impact. Compos Struct 2016;149:408–22. http://dx.doi.org/10.1016/j.compstruct.2016.04.012, URL https://www.sciencedirect.com/science/article/pii/S0263822316302513.

[14] Puck A, Schürmann H. Failure analysis of FRP laminates by means of physically based phenomenological models. Compos Sci Technol 2002;62(12):1633–62. http://dx.doi.org/10.1016/S0266-3538(01)00208-1, URL https://www.sciencedirect.com/science/article/pii/S0266353801002081.

[15] Camanho P, Arteiro A, Melro A, Catalanotti G, Vogler M. Three-dimensional invariant-based failure criteria for fibre-reinforced composites. Int J Solids Struct 2015;55:92–107. http://dx.doi.org/10.1016/j.ijsolstr.2014.03.038, Special Issue Computational and Experimental Mechanics of Advanced Materials A workshop held at King Abdullah University of Science and Technology Jeddah, Kingdom of Saudi Arabia July 1-3, 2013, URL https://www.sciencedirect.com/science/article/pii/S0020768314001449.

[16] Pinho S, Darvizeh R, Robinson P, Schuecker C, Camanho P. Material and structural response of polymer-matrix fibre-reinforced composites. J Compos Mater 2012;46(19–20):2313–41. http://dx.doi.org/10.1177/0021998312454478, arXiv:https://doi.org/10.1177/0021998312454478.

[17] Catalanotti G, Camanho P, Marques A. Three-dimensional failure criteria for fiber-reinforced laminates. Compos Struct 2013;95:63–79. http://dx.doi.org/10.1016/j.compstruct.2012.07.016, URL https://www.sciencedirect.com/science/article/pii/S0263822312003443.

[18] Hashin Z. Failure Criteria for Unidirectional Fiber Composites. J Appl Mech 1980;47(2):329–34. http://dx.doi.org/10.1115/1.3153664, arXiv:https://asmedigitalcollection.asme.org/appliedmechanics/article-pdf/47/2/329/5878334/329_1.pdf.

[19] Chang F-K, Chang K-Y. A progressive damage model for laminated composites containing stress concentrations. J Compos Mater 1987;21(9):834–55.

[20] Rozylo P, Debski H. Stability and load-carrying capacity of short composite Z-profiles under eccentric compression. Thin-Walled Struct 2020;157:107019. http://dx.doi.org/10.1016/j.tws.2020.107019, URL https://www.sciencedirect.com/science/article/pii/S0263823120308946.

[21] Rozylo P. Comparison of failure for thin-walled composite columns. Materials 2022;15(1). http://dx.doi.org/10.3390/ma15010167, URL https://www.mdpi.com/1996-1944/15/1/167.

[22] Rozylo P. Failure phenomenon of compressed thin-walled composite columns with top-hat cross-section for three laminate lay-ups. Compos Struct 2023;304:116381. http://dx.doi.org/10.1016/j.compstruct.2022.116381, URL https://www.sciencedirect.com/science/article/pii/S0263822322011138.

[23] Riccio A, Saputo S, Sellitto A, Di Caprio F. On the crashworthiness behaviour of a composite fuselage sub-floor component. Compos Struct 2020;234:111662. http://dx.doi.org/10.1016/j.compstruct.2019.111662, URL https://www.sciencedirect.com/science/article/pii/S0263822319338358.

[24] Riccio A, Saputo S, Sellitto A, Di Caprio F, Di Palma L. A numerical-experimental assessment on a composite fuselage barrel vertical drop test: Induced damage onset and evolution. Compos Struct 2020;248:112519. http://dx.doi.org/10.1016/j.compstruct.2020.112519, URL https://www.sciencedirect.com/science/article/pii/S0263822320314847.

[25] Gransden DI, Alderliesten R. Development of a finite element model for comparing metal and composite fuselage section drop testing. Int J Crashworthiness 2017;22(4):401–14. http://dx.doi.org/10.1080/13588265.2016.1273987, arXiv:https://doi.org/10.1080/13588265.2016.1273987.

[26] Perfetto D, De Luca A, Lamanna G, Chiariello A, Di Caprio F, Di Palma L, et al. Drop test simulation and validation of a full composite fuselage section of a regional aircraft. Procedia Struct Integr 2018;12:380–91. http://dx.doi.org/10.1016/j.prostr.2018.11.079, AIAS 2018 international conference on stress analysis, URL https://www.sciencedirect.com/science/article/pii/S2452321618301823.

[27] Caputo F, Lamanna G, Perfetto D, Chiariello A, Di Caprio F, Di Palma L. Experimental and numerical crashworthiness study of a full-scale composite fuselage section. AIAA J 2021;59(2):700–18. http://dx.doi.org/10.2514/1.J059216, arXiv:https://doi.org/10.2514/1.J059216.

[28] Milan C, Giannopoulos IK, Theotokoglou EE. Crashworthiness behaviour of a composite fuselage section with cargo door. In: Proceedings of the 10th GRACM international congress on computational mechanics. 2021.

[29] Mou H, Xie J, Feng Z. Research status and future development of crashworthiness of civil aircraft fuselage structures: An overview. Prog Aerosp Sci 2020;119:100644. http://dx.doi.org/10.1016/j.paerosci.2020.100644, URL https://www.sciencedirect.com/science/article/pii/S0376042120300567.

[30] Koerber H, Camanho P. High strain rate characterisation of unidirectional carbon–epoxy IM7-8552 in longitudinal compression. Composites A 2011;42(5):462–70. http://dx.doi.org/10.1016/j.compositesa.2011.01.002, URL https://www.sciencedirect.com/science/article/pii/S1359835X11000054.

[31] Raimondo L, Iannucci L, Robinson P, Curtis P. Modelling of strain rate effects on matrix dominated elastic and failure properties of unidirectional fibre-reinforced polymer–matrix composites. Compos Sci Technol 2012;72(7):819–27. http://dx.doi.org/10.1016/j.compscitech.2012.02.011, URL https://www.sciencedirect.com/science/article/pii/S026635381200070X.

[32] Kwon Y, Panick C. Strain rate dependent failure criteria for fibrous composites using multiscale approach. Multiscale Multidiscip Model Exp Des 2020;3. http://dx.doi.org/10.1007/s41939-019-00055-0.

[33] Daniel I, Werner B, Fenner J. Strain-rate-dependent failure criteria for composites. Compos Sci Technol 2011;71(3):357–64. http://dx.doi.org/10.1016/j.compscitech.2010.11.028, URL https://www.sciencedirect.com/science/article/pii/S0266353810004677.

[34] Millen S, Murphy A, Catalanotti G, Abdelal G. Coupled thermal-mechanical progressive damage model with strain and heating rate effects for lightning strike damage assessment. Appl Compos Mater 2019;26. http://dx.doi.org/10.1007/s10443-019-09789-z.

[35] Chen Y, Hou S, Fu K, Han X, Ye L. Low-velocity impact response of composite sandwich structures: Modelling and experiment. Compos Struct 2017;168:322–34. http://dx.doi.org/10.1016/j.compstruct.2017.02.064, URL https://www.sciencedirect.com/science/article/pii/S0263822316321110.

[36] Wang K, Zhao L, Hong H, Zhang J. A strain-rate-dependent damage model for evaluating the low velocity impact induced damage of composite laminates. Compos Struct 2018;201:995–1003. http://dx.doi.org/10.1016/j.compstruct.2018.06.046, URL https://www.sciencedirect.com/science/article/pii/S0263822318305853.

[37] Liu X, Bai C, Xi X, Zhou S, Zhang X, Li X, et al. Impact response and crashworthy design of composite fuselage structures: An overview. Prog Aerosp Sci 2024;101002. http://dx.doi.org/10.1016/j.paerosci.2024.101002, URL https://www.sciencedirect.com/science/article/pii/S0376042124000289.

[38] Shao JR, Liu N, Zheng ZJ. A modified progressive damage model for simulating low-velocity impact of composite laminates. Adv Mech Eng 2022;14(5):16878132221095948. http://dx.doi.org/10.1177/16878132221095948, arXiv:https://doi.org/10.1177/16878132221095948.

[39] Zhou J, Wen P, Wang S. Finite element analysis of a modified progressive damage model for composite laminates under low-velocity impact. Compos Struct 2019;225:111113. http://dx.doi.org/10.1016/j.compstruct.2019.111113, URL https://www.sciencedirect.com/science/article/pii/S0263822319303976.

[40] Matzenmiller A, Lubliner J, Taylor R. A constitutive model for anisotropic damage in fiber-composites. Mech Mater 1995;20(2):125–52. http://dx.doi.org/10.1016/0167-6636(94)00053-0, URL https://www.sciencedirect.com/science/article/pii/0167663694000530.

[41] Zhang H, Sun J, Rui X, Liu S. Delamination damage imaging method of CFRP composite laminate plates based on the sensitive guided wave mode. Compos Struct 2023;306:116571. http://dx.doi.org/10.1016/j.compstruct.2022.116571, URL https://www.sciencedirect.com/science/article/pii/S0263822322013034.

[42] Senthil K, Arockiarajan A, Palaninathan R, Santhosh B, Usha K. Defects in composite structures: Its effects and prediction methods – A comprehensive review. Compos Struct 2013;106:139–49. http://dx.doi.org/10.1016/j.compstruct.2013.06.008, URL https://www.sciencedirect.com/science/article/pii/S0263822313002845.

[43] Dassault Systèmes. SIMULIA User Assistance 2023. 2023.

[44] Wu EM, Reuter RC. Crack extension in fiberglass reinforced plastics. 1965.

[45] Benzeggagh M, Kenane M. Measurement of mixed-mode delamination fracture toughness of unidirectional glass/epoxy composites with mixed-mode bending apparatus. Compos Sci Technol 1996;56(4):439–49. http://dx.doi.org/10.1016/0266-3538(96)00005-X, URL https://www.sciencedirect.com/science/article/pii/026635389600005X.

[46] Shi Y, Swait T, Soutis C. Modelling damage evolution in composite laminates subjected to low velocity impact. Compos Struct 2012;94(9):2902–13. http://dx.doi.org/10.1016/j.compstruct.2012.03.039, URL https://www.sciencedirect.com/science/article/pii/S0263822312001547.

[47] Riccio A, Raimondo A, Di Caprio F, Fusco M, Sanità P. Experimental and numerical investigation on the crashworthiness of a composite fuselage sub-floor support system. Composites B 2018;150:93–103. http://dx.doi.org/10.1016/j.compositesb.2018.05.044, URL https://www.sciencedirect.com/science/article/pii/S1359836818306668.

[48] Di Caprio F, Ignarra M, Marulo F, Guida M, Lamboglia A, Gambino B. Design of composite stanchions for the cargo subfloor structure of a civil aircraft. Procedia Eng 2016;167:88–96. http://dx.doi.org/10.1016/j.proeng.2016.11.673, International Symposium on Dynamic Response and Failure of Composite materials, Draf2016, URL https://www.sciencedirect.com/science/article/pii/S1877705816340310.

[49] Sellitto A, Di Caprio F, Guida M, Saputo S, Riccio A. Dynamic pulse buckling of composite stanchions in the sub-Cargo Floor Area of a civil regional aircraft. Materials 2020;13(16). http://dx.doi.org/10.3390/ma13163594, URL https://www.mdpi.com/1996-1944/13/16/3594.

[50] Zhang X, Li Z, Yang Z, Jiang L, Pan G. Buckling of composite shells with a novel initial imperfection model subjected to hydrostatic pressure. Compos Struct 2022;297:115949. http://dx.doi.org/10.1016/j.compstruct.2022.115949, URL https://www.sciencedirect.com/science/article/pii/S0263822322007061.

[51] Zhenyu F, Jiang X, Shanshan S, Haolei M, Xuan S, Xuehan Z. The failure mechanism and energy-absorbing characteristics of composite thin-walled C-channels subject to low-speed axial compression. J Compos Mater 2019;53(16):2249–59. http://dx.doi.org/10.1177/0021998319826337, arXiv:https://doi.org/10.1177/0021998319826337.

[52] Hsiao H, Daniel I. Strain rate behavior of composite materials. Composites B 1998;29(5):521–33. http://dx.doi.org/10.1016/S1359-8368(98)00008-0, URL https://www.sciencedirect.com/science/article/pii/S1359836898000080.

[53] Perry J, Walley S. Measuring the effect of strain rate on deformation and damage in fibre-reinforced composites: A review. J Dyn Behav Mater 2022;8. http://dx.doi.org/10.1007/s40870-022-00331-0.

[54] Bussadori B, Schuffenhauer K, Scattina A. Modelling of CFRP crushing structures in explicit crash analysis. Composites B 2014;60:725–35. http://dx.doi.org/10.1016/j.compositesb.2014.01.020, URL https://www.sciencedirect.com/science/article/pii/S1359836814000304.